CMB-S4: Forecasting Constraints on f_{NL} Through μ -distortion Anisotropy

David Zegeve, ^{1,2,*} Federico Bianchini, ³ J. Richard Bond, ⁴ Jens Chluba, ⁵ Thomas Crawford, ^{1,2} Giulio Fabbian, ^{6,7} Vera Gluscevic, ⁸ Daniel Grin, ⁹ J. Colin Hill, ¹⁰ P. Daniel Meerburg, ¹¹ Giorgio Orlando, ¹¹ Bruce Partridge, ⁹ Christian L. Reichardt, ¹² Mathieu Remazeilles, ¹³ Douglas Scott, ¹⁴ Edward J. Wollack, ¹⁵ and The CMB-S4 Collaboration ¹Department of Astronomy & Astrophysics, The University of Chicago, Chicago, IL 60637, USA ²Kavli Institute for Cosmological Physics, The University of Chicago, Chicago, IL 60637, USA ³Kavli Institute for Particle Astrophysics and Cosmology, Stanford University, 452 Lomita Mall, Stanford, California 94305, USA ⁴Canadian Institute for Theoretical Astrophysics, 60 St. George Street, University of Toronto, Toronto, ON, M5S 3H8, Canada ⁵ Jodrell Bank Centre for Astrophysics, Alan Turing Building, University of Manchester, Manchester M13 9PL ⁶ Center for Computational Astrophysics, Flatiron Institute, 162 5th Avenue, New York, NY 10010, USA ⁷School of Physics and Astronomy, Cardiff University, The Parade, Cardiff, CF24 3AA, UK ⁸ Department of Physics and Astronomy, University of Southern California, Los Angeles, California 90089, USA ⁹Department of Physics and Astronomy, Haverford College, 370 Lancaster Avenue, Haverford, PA 19041, USA ¹⁰Department of Physics, Columbia University, New York, New York 10027, USA ¹¹ Van Swinderen Institute for Particle Physics and Gravity, University of Groningen, Nijenborgh 4, 9747 AG Groningen, The Netherlands ¹²School of Physics, University of Melbourne, Parkville, VIC 3010, Australia ¹³Instituto de Fisica de Cantabria (CSIC-UC), Avda. los Castros s/n, 39005 Santander, Spain ¹⁴Department of Physics and Astronomy, University of British Columbia, 6225 Agricultural Road, Vancouver, BC V6T 1Z1, Canada ¹⁵NASA/Goddard Space Flight Center, Greenbelt, MD 20771, USA (Dated: March 3, 2023)

Diffusion damping of the cosmic microwave background (CMB) power spectrum results from imperfect photon-baryon coupling in the pre-recombination plasma. At redshift $5 \times 10^4 < z < 2 \times 10^6$. the plasma acquires an effective chemical potential, and energy injections from acoustic damping in this era create μ -type spectral distortions of the CMB. These μ distortions trace the underlying photon density fluctuations, probing the primordial power spectrum in short-wavelength modes $k_{\rm S}$ over the range 50 Mpc⁻¹ $\lesssim k \lesssim 10^4$ Mpc⁻¹. Small-scale power modulated by long-wavelength modes $k_{\rm L}$ from squeezed-limit non-Gaussianities introduces cross-correlations between CMB temperature anisotropies and μ distortions. Under single-field inflation models, $\mu \times T$ correlations measured from an observer in an inertial frame should vanish up to a factor of $(k_L/k_S)^2 \ll 1$. Thus, any measurable correlation rules out single-field inflation models. We forecast how well the next-generation groundbased CMB experiment CMB-S4 will be able to constrain primordial squeezed-limit non-Gaussianity, parameterized by $f_{\rm NL}$, using measurements of $C_\ell^{\mu T}$ as well as $C_\ell^{\mu E}$ from CMB E modes. Using current experimental specifications and foreground modeling, we expect $\sigma(f_{\rm NL}) \lesssim 1000$. This is roughly four times better than the current limit on $f_{\rm NL}$ using $\mu \times T$ and $\mu \times E$ correlations from Planck and is comparable to what is achievable with LiteBIRD, demonstrating the power of the CMB-S4 experiment. This measurement is at an effective scale of $k \simeq 740 \; \mathrm{Mpc}^{-1}$ and is thus highly complementary to measurements at larger scales from primary CMB and large-scale structure.

I. INTRODUCTION

The paradigm of cosmic inflation presents arguably the most compelling and plausible scenario for the earliest moments of the existence of our Universe and provides a mechanism for creating the den-

sity perturbations that have grown under the influence of gravity to form all the structure we see in the Universe today. (For an overview of the theoretical background and observational evidence for inflation, see, e.g., the review by Ellis & Wands in Chapter 23 in Ref. [78].) If a period of inflation did occur, observations of the cosmic microwave background (CMB) and tracers of the density field can give us clues about the nature of the fields involved in inflation and their dynamics. By extension, these

^{*} dzegeye@uchicago.edu

observations can probe physics at the energy scale of the inflationary potential, far beyond the energy reach of any terrestrial experiment. The CMB has most famously been used to constrain inflation models through measurements of the power spectrum of density fluctuations and constraints on the imprint of inflationary gravitational-wave background on the polarization of the CMB (e.g., [5]), but CMB observations can also shed light on inflationary dynamics through searches for signatures of primordial non-Gaussianity (PNG, e.g., [4, 10, 12–15, 23–25, 34, 67, 69, 76]).

The most well-studied form of PNG is the socalled squeezed-limit bispectrum (or Fourier-domain three-point function), which describes a configuration of triangles in Fourier space in which two of the k modes have a much larger value than the third. This corresponds to a real-space configuration in which a long-wavelength mode modulates the amplitude of small-scale fluctuation power. Mathematically, this is usually expressed in terms of the relationship of the bispectrum of curvature perturbations to the curvature power spectrum (e.g., [70]):

$$B_{\zeta}(k_1, k_2, k_3)_{k_3 \ll k_1 \simeq k_2} = \frac{12}{5} f_{\text{NL}} P_{\zeta}(k_1) P_{\zeta}(k_3), \quad (1)$$

where $f_{\rm NL}$ parameterizes the amplitude of local non-Gaussianity and is defined explicitly through the first-order expression for real-space local PNG:

$$\zeta(x) = \zeta_g + \frac{3}{5} f_{\rm NL}(\zeta_g^2 - \langle \zeta_g^2 \rangle), \tag{2}$$

where ζ_g is a random Gaussian field. One of the reasons the squeezed-limit configuration is so well-studied is that models of inflation with a single scalar field whose kinetic energy is always much less than its potential energy ("single-field, slow-roll inflation") produce vanishingly small amounts of PNG of the squeezed-limit type [33]. A detection of this type of PNG at levels of $f_{\rm NL} \gtrsim 0.01$ would thus rule out large classes of inflation models, including many of the most popular and viable models (e.g., [3]).

The best current limits on the value of $f_{\rm NL}$ in the squeezed limit come from analyses of the primary CMB from the *Planck* satellite [9]: $f_{\rm NL} = -0.9 \pm 5.1$ (68% CL). Even cosmic-variance-limited maps of the CMB temperature and polarization out to $\ell = 4000$ would only improve these limits by roughly a factor of five [47]. Interest is thus high in other methods of determining $f_{\rm NL}$. From a pure mode-counting perspective, there is much more information in the distribution of matter in the local and moderate-redshift Universe, but the non-Gaussianity caused by non-linear growth complicates bispectrum measurements of the galaxy distribution significantly.

Previous work has shown that squeezed-limit PNG causes a unique scale-dependent bias in the galaxy distribution [35], and this signature is a target of upcoming galaxy surveys (e.g., [11]), as is a direct measurement of the matter bispectrum supplanted with careful modeling (e.g., [40]).

Another promising avenue for detecting or constraining local PNG involves distortions to the blackbody spectrum of the CMB [18, 26, 46, 74]. Injections of energy into the primordial plasma will distort the spectrum of the CMB, and a known source of energy release in the early Universe is the dissipation of small-scale acoustic waves [31, 36, 45, 73] from photon diffusion or Silk damping [68]. The authors of Refs. [42, 61] pointed out that a modulation of small-scale power by long-wavelength modes that underlie squeezed-limit PNG would result in anisotropy in the μ distortion and that a cosmicvariance-limited measurement of the μ -distortion - temperature cross-spectrum ($\mu \times T$) could limit local-type PNG to $f_{\rm NL}\lesssim 10^{-3}$. Furthermore, because the μ -distortion signal is created by perturbations with wavenumbers $k \simeq 50 - 10^4 \, \mathrm{Mpc}^{-1}$, scales that are inaccessible by other cosmological probes [30, 31, 49], constraints on f_{NL} from $\mu \times T$ are highly complementary to constraints on large-scale PNG from primary CMB or even large-scale structure.

In Refs. [63, 65], the authors performed realistic forecasting for the limits on $f_{\rm NL}$ using μ -distortion anisotropy measurements from proposed space missions, including the effects of foreground contamination. Similar methods have also been used to derive limits on PNG from Planck [48, 66] and COBE/FIRAS [17], with the most stringent limit, $f_{\rm NL} \lesssim 6800$ (95% C.L.), coming from Ref. [66].

In this work we consider the potential of measuring μ -distortion anisotropy from the ground. Ground-based measurements have not been considered in previous works, mainly because the calibration and stability requirements for measuring the global μ signal are so stringent that it has been assumed that only in the exquisitely stable environment of space, with no intervening atmosphere, would such a measurement be possible. Following Ref. [42], we point out in this work that measuring the μ -distortion anisotropy is a fundamentally different task. Since anisotropy measurements can be made with a differencing radiometer, most of the stability and calibration requirements are converted to requirements on instantaneous sensitivity.

In this work we focus on the potential of the upcoming CMB-S4 experiment [1] to measure μ -distortion anisotropy—specifically, the correlation between μ and CMB temperature and polarization anisotropies. We calculate the constraints on $f_{\rm NL}$ from CMB-S4 $\mu \times T$ and $\mu \times E$ measurements, first

considering raw sensitivity alone then adding the effects of atmospheric contamination and foregrounds.

The paper is organized as follows. We discuss the theoretical background in Section II; we describe the methods we use for forecasting in Section III; we present the survey configuration for CMB-S4 in Section IV; we present our results in Section V; and we conclude in Section VI.

II. BACKGROUND

In this section, we review some of the key theoretical concepts in calculating and forecasting the $\mu \times T$ and $\mu \times E$ correlation arising from squeezed-limit non-Gaussianity.

A. Power Spectrum and Bispectrum

In the limit of purely Gaussian-distributed primordial curvature perturbations $\zeta(\vec{k})$, the autocorrelation of these perturbations is given by

$$\left\langle \zeta_{\vec{k}_1} \zeta_{\vec{k}_2} \right\rangle = (2\pi)^3 \delta \left(\vec{k}_1 + \vec{k}_2 \right) P_{\zeta} \left(k_1 \right). \tag{3}$$

The power spectrum $P_{\zeta}(k)$ of these perturbations from single-field inflation models is given by

$$P_{\zeta}(k) = \frac{2\pi^2}{k^3} \Delta_{\zeta}^2(k), \quad \Delta_{\zeta}^2(k) \equiv A_s \left(\frac{k}{k_{\rm p}}\right)^{n_{\rm s}-1}. \quad (4)$$

Here we use best-fit numbers from the *Planck* 2018 data release [8]: $A_{\rm s}=2.1\times 10^{-9};$ and $n_{\rm s}=0.965,$ reported for a pivot scale $k_{\rm p}=0.05~{\rm Mpc}^{-1}.$

In the squeezed limit, where the global power spectrum of two modes on short scales $k_{\rm S}$ are modulated by a long-wavelength mode $k_{\rm L}$, the long-wavelength modes generate a local non-Gaussianity and the power spectrum becomes position-dependent

$$P_{\zeta}(k_{\rm S}, x) = P_{\zeta}(k_{\rm S}) \left[1 + \frac{d \ln P_{\zeta}(k_{\rm S})}{d\zeta_{\rm L}} \zeta_{\rm L}(x) \right]. \quad (5)$$

One common measure of the level of non-Gaussianity in the curvature distribution is the Fourier-domain statistic known as the curvature bispectrum $B_{\zeta}(k_1,k_2,k_3)$. Analogous to the power spectrum and the auto-correlation, the bispectrum is defined through its relationship to the three-point correlation function:

$$\left\langle \zeta_{\vec{k}_1} \zeta_{\vec{k}_2} \zeta_{\vec{k}_3} \right\rangle = (2\pi)^3 \delta \left(\vec{k}_1 + \vec{k}_2 + \vec{k}_3 \right) B_{\zeta}(k_1, k_2, k_3).$$
 (6)

In the squeezed limit, $k_1/k_3 \rightarrow 0$, the bispectrum can be expressed as in Eq. (1), with $f_{\rm NL}$ parameterizing the amount of local non-Gaussianity coupling the power spectrum at long and short wavelengths. In the squeezed limit, $f_{\rm NL}$ obeys a consistency relationship with the primordial power spectrum [56]:

$$\lim_{k_{\rm L}/k_{\rm S} \to 0} \frac{12}{5} f_{\rm NL}(k_{\rm L}, k_{\rm S}, k_{\rm S}) = -\frac{d \ln \Delta_{\zeta}^2(k_{\rm S})}{d \ln k_{\rm S}}.$$
 (7)

For slow-roll single-field inflation, the consistency relationship becomes

$$\lim_{k_{\rm L}/k_{\rm S} \to 0} \frac{12}{5} f_{\rm NL} (k_{\rm L}, k_{\rm S}, k_{\rm S}) = 1 - n_{\rm s}.$$
 (8)

For the specific observable $\mu \times T$, however, the type of PNG produced in single-field inflation results in a vanishingly small signal, far below what is predicted by the consistency relation [21, 61]. This means any measurable signal of $\mu \times T$ would rule out single-field inflation models. We review the reasoning behind this result in Section II C 1.

B. μ distortions

In the early Universe, energy injected into the plasma will efficiently thermalize through double Compton scattering and bremsstrahlung, producing a blackbody distribution with a new temperature. These two processes are highly efficient until a redshift $z_i \simeq 2 \times 10^6$, at which point the Universe has expanded enough that the density necessary for double Compton and bremsstrahlung to frequently occur becomes too low [46]. This leaves elastic Compton scattering, which conserves photon number, as the primary method for the photon-baryon bath to reach thermal equilibrium. The inefficient thermalization introduces a chemical potential, where the mixing of different blackbody spectra at different temperatures produces a Bose-Einstein rather than Planckian distribution [80]. At small chemical potentials, the Bose-Einstein distribution can be approximated as a distorted blackbody spectrum in which

$$n(\nu) = \left[e^{h\nu/(k_{\rm B}T)} - 1\right]^{-1} \to \left[e^{h\nu/(k_{\rm B}T) + \mu} - 1\right]^{-1},$$
(9)

where h is Planck's constant and $k_{\rm B}$ is Boltzmann's constant. This distortion of the CMB spectrum from a typical blackbody is known as a μ -type distortion. It occurs until a redshift $z_{\rm f} \simeq 5 \times 10^4$, where even thermalization through single Compton becomes inefficient and distortions of the y-type start being produced [28].

 μ distortions can be generated from a variety of mechanisms. The primary contribution we will consider in this work is from diffusion damping of small-scale power. The μ distortions produced by diffusion damping can be related to the primordial curvature perturbations via

$$\mu(x) = \int_{\vec{k}_1} \int_{\vec{k}_2} \zeta(\vec{k}_1) \zeta(\vec{k}_2) W(\vec{k}_1, \vec{k}_2) e^{i(\vec{k}_1 + \vec{k}_2) \cdot \vec{x}},$$
(10)

where $W(\vec{k}_1, \vec{k}_2)$, the window function, captures the weighted amount of dissipated modes with wavenumber k [21, 29, 79]. To relate the amount of μ distortions to the primordial power spectrum, we take the ensemble average of $\mu(x)$ and $k_1 = k_2$

$$\langle \mu(x) \rangle \simeq \frac{1}{2\pi^2} \int dk P_{\zeta}(k) k^2 W(k).$$
 (11)

Assuming that μ distortions are generated from subhorizon modes at the time of dissipation, the window function is

$$W(k) \approx -4.54k^2 \int_0^\infty dz \frac{dk_{\rm D}^{-2}}{dz} \mathcal{J}_{\mu}(z) e^{-\frac{2k^2}{k_{\rm D}^2(z)}},$$
 (12)

where $k_{\rm D}$ is the damping scale for energy injection from diffusion damping,

$$k_{\rm D}(z) \approx 4.1 \times 10^{-6} (1+z)^{3/2} \rm Mpc^{-1},$$
 (13)

and \mathcal{J}_{μ} is the time window function for μ distortions [21, 29, 79]. The time window function is well approximated by an analytical Green's function given in Ref. [27]

$$\mathcal{J}_{\mu}(z) \approx \left[1 - \exp\left(-\left[\frac{1+z}{5.8 \times 10^4}\right]^{1.88}\right)\right] \times e^{-(z/z_i)^{5/2}},\tag{14}$$

where $z_i \simeq 2 \times 10^6$ is defined above as the beginning of the μ -distortion era. For single-field, slow-roll inflation, the average amount of μ distortions is roughly $\langle \mu(x) \rangle \simeq 2 \times 10^{-8}$ [20, 28, 31]. We find that μ distortions are tracers of primordial perturbations in the range 50 Mpc⁻¹ $\lesssim k_{\mu} \lesssim 1 \times 10^4$ Mpc⁻¹ [20, 28, 31].

C. μ cross-correlations

Anisotropies of the CMB probe the primordial curvature perturbations of inflation. CMB anisotropies are typically decomposed into spherical harmonics. For example, the real-space temperature anisotropy field $\Theta(\hat{n}) = \delta T(\hat{n})/T$, can be decomposed into spherical harmonics $\Theta(\hat{n}) = \delta T(\hat{n})/T$

 $\sum_{\ell m} a_{\ell m}^T Y_{\ell m}(\hat{n})$. The spherical harmonic coefficients of the various CMB anisotropy fields are related to (Fourier-space) primordial curvature perturbations through

$$a_{\ell m}^{X} = 4\pi i^{-\ell} \int_{\vec{k}} e^{i\vec{k}\cdot\vec{x}} \zeta(\vec{k}) \Delta_{\ell}^{X}(k) Y_{\ell m}^{*}(\vec{k}),$$
 (15)

where X denotes the type of CMB anisotropy field (we are considering only T and E here), and $\Delta_{\ell}^{X}(k)$ is the transfer function connecting primordial perturbations to CMB anisotropies. The coefficients can then be correlated with each other:

$$\left\langle \left(a_{\ell m}^X \right)^* a_{\ell' m'}^Y \right\rangle = \delta_{\ell \ell'} \delta_{m m'} C_{\ell}^{XY},$$
 (16)

where C_{ℓ}^{XY} is the angular cross-power spectrum of CMB anisotropy fields X and Y.

Observations of μ -distortion anistropies can also be decomposed into spherical harmonics:

$$a_{\ell m}^{\mu} = 4\pi i^{-\ell} \int_{\vec{k}} e^{i\vec{k}\cdot\vec{x}} \mu(\vec{k}) \Delta_{\ell}^{\mu}(k) Y_{\ell m}^{*}(\vec{k}),$$
 (17)

where $\Delta_{\ell}^{\mu}(k)$ is the transfer function of anisotropic μ distortions [21]:

$$\Delta_{\ell}^{\mu}(k) = e^{-k^2/\left(q_{\mu,D}^2(z_{\text{rec}})\right)} j_{\ell}(k\Delta\eta) \qquad (18)$$
$$\Delta\eta \equiv \eta_0 - \eta_{\text{rec}}$$
$$q_{\mu,D}(z_{\text{rec}}) \simeq 0.084 \,\text{Mpc}^{-1},$$

and η_0 and $\eta_{\rm rec}$ are the conformal times corresponding to z=0 and the redshift of recombination $z=z_{\rm rec}$, respectively. The angular correlation of μ distortions with CMB anisotropies is then given by

$$\left\langle a_{\ell m}^{\mu} \left(a_{\ell' m'}^{X} \right)^{*} \right\rangle = \delta_{\ell \ell'} \delta_{m m'} C_{\ell}^{\mu X} =$$

$$(4\pi)^{2} i^{-\ell+\ell'} \int_{\vec{k}_{S}} \int_{\vec{k}_{L}} e^{i(\vec{k}_{S} - \vec{k}_{L}) \cdot \vec{x}} \times$$

$$\left\langle \mu \left(\vec{k}_{S} \right) \zeta(-\vec{k}_{L}) \right\rangle \Delta_{\ell}^{\mu} (\vec{k}_{S}) \Delta_{\ell'}^{X} (\vec{k}_{L}) Y_{\ell m}^{*} (\hat{k}_{S}) Y_{\ell' m'} (\hat{k}_{L}),$$

$$(19)$$

where we have explicitly indicated here that, because of the very different transfer functions, this correlation probes the connection of the curvature power on very small scales through $\mu(\vec{k}_{\rm S})$ with the large-scale curvature $\zeta(\vec{k}_{\rm L})$. In other words, this measurement is sensitive to the correlation of a large-scale mode with two extremely small-scale modes, i.e., the bispectrum in the ultra-squeezed limit. The non-Gaussianities being probed are at scales of $50~{\rm Mpc}^{-1} \lesssim k_{\mu} \lesssim 1 \times 10^4~{\rm Mpc}^{-1}$, much smaller than scales probed by Planck measurements of the primary CMB [9].

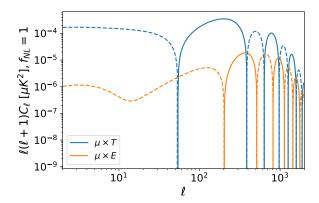


FIG. 1. Angular cross-power spectrum of $\mu \times T$ and $\mu \times E$ for $\langle \mu \rangle = 2 \times 10^{-8}$ and $f_{\rm NL} = 1$. Solid lines correspond to positive values while dashed lines correspond to negative values.

The ensemble average of $\left\langle \mu \left(\vec{k}_{\mathrm{S}} \right) \zeta (-\vec{k}_{\mathrm{L}}) \right\rangle$ is

$$\left\langle \mu \left(\vec{k}_{\rm S} \right) \zeta (-\vec{k}_{\rm L}) \right\rangle = \left\langle \mu \right\rangle P_{\zeta}(k_{\rm L}) \frac{12}{5} f_{\rm NL}.$$
 (20)

We use this to re-express $C_{\ell}^{\mu X}$ as

$$C_{\ell}^{\mu X} = \frac{24\langle \mu \rangle}{5\pi} f_{\rm NL} \int_0^{+\infty} \mathrm{d}k P_{\zeta}(k) k^2 \Delta_{\ell}^{\mu}(k) \Delta_{\ell}^{X}(k). \tag{21}$$

The angular power spectra $C_\ell^{\mu T}$ and $C_\ell^{\mu E}$ for $\langle \mu \rangle = 2 \times 10^{-8}$ and $f_{\rm NL} = 1$ are plotted in Figure 1.

1. $\mu \times T$ in single-field inflation

As discussed in Section II A, even in single-field inflation, squeezed-limit non-Gaussianity can be generated at the level of $f_{\rm NL} \sim 1-n_s$, where n_s is the spectral index of the curvature power spectrum [56]. The mechanism that produces this squeezed-limit non-Gaussianity, however, produces vanishingly small amounts (far smaller than the level of $f_{\rm NL} = 1-n_s$) of $\mu \times T$ correlations. For this reason, $\mu \times T$ measurements have the potential to rule out single-field inflation more stringently than other probes. This was recognized by the authors of Ref. [21]; we briefly summarize their argument here.

In single-field inflation, squeezed-limit non-Gaussianity is produced by long-wavelength modes that are outside of the Hubble radius modulating the global small scale power spectrum by acting as a modulation of the global scale, or a coordinate transformation, as seen in Eq. (5). For μ distortions, this results in a shift in the observed value of μ in direc-

tion \hat{n} of the form:

$$\mu\left(\hat{n}\right) = \mu\left(z_f, \vec{x}_{\text{rec}}\right) + \zeta_L\left(z_f, \vec{x}_{\text{rec}}\right) \hat{n} \cdot \nabla_{\hat{n}} \mu\left(z_f, \vec{x}_{\text{rec}}\right), \tag{22}$$

where $\vec{x}_{\rm rec} = \hat{n}(\eta_0 - \eta_{\rm rec})$. However, the value of μ distortion at a given position is a local phenomenon and only traces the amount of power dissipated, which in turn depends on the value of the local small-scale power spectrum, which is invariant in the case of no other form of modulation. Thus, $\mu(\vec{x}) = \langle \mu \rangle$, and, relating the long wavelength mode ζ_L to the large-scale temperature anisotropy via $\zeta_L = -\frac{9}{2}\Theta_L$, in the Sachs-Wolfe approximation [21], we can write

$$\mu(\hat{n}) \sim \langle \mu \rangle + \Theta_L \hat{n} \cdot \nabla_{\hat{n}} \langle \mu \rangle,$$

$$= \langle \mu \rangle + 0,$$
(23)

This makes it clear that μ distortions from diffusion damping cannot correlate with a long wavelength temperature mode via this mechanism:

$$\langle \mu T \rangle \sim \langle \Theta_{\rm L} \rangle \langle \mu \rangle + \langle \Theta_{\rm L}^2 \rangle \nabla_{\hat{n}} \langle \mu \rangle = \langle \Theta_{\rm L} \rangle \langle \mu \rangle = 0.$$
(24)

This means that $\mu \times T$ is vanishingly small from non-Gaussianity in single-field inflation, and the only terms that survive are ones with $(k_{\rm L}/k_{\rm S})^2$ suppression [21]. Therefore, any measurable signal of $\mu \times T$ would rule out single-field models. This similarly applies to $\mu \times E$.

III. METHODS

Our aim is to forecast constraints on $f_{\rm NL}$ using joint analysis of $\mu \times T$ and $\mu \times E$ correlations from CMB-S4. In this section, we will describe the key techniques we use to forecast sensitivity. First we describe the Fisher-matrix formalism used to convert μ , T, and E power spectra to constraints on $f_{\rm NL}$. We then describe the component-separation technique that allows us to predict μ and T or E power spectra given the total signal + noise + foreground covariance matrix for a particular experimental configuration. Finally, we describe how we model the noise and foreground contributions to the band-band covariance matrix.

A. Fisher Matrix

If we would like to know how accurately we can measure a given parameter p_i in a data set, we can assume the likelihood \mathcal{L} of measuring the parameter follows a Gaussian distribution:

$$\mathcal{L} \propto \exp\left[-\frac{1}{2}\left(p_i - \hat{p}_i\right)F_{ij}\left(p_j - \hat{p}_j\right)\right], \quad (25)$$

where p_i is a fiducial value of the parameter and \hat{p}_i is the measured value. F_{ij} is the Fisher matrix, which captures the covariance of measured parameters. We discuss the validity of the assumption of Gaussian likelihood in Section III B.

We make the approximation that the amplitude of the $\mu \times T$ and $\mu \times E$ spectra are controlled by a single free parameter $f_{\rm NL}$ and write

$$C_{\ell}^{\mu X} = f_{\rm NL} C_{\ell}^{\mu X} \Big|_{f_{\rm NL}=1}$$
 (26)

The Fisher "matrix" in this case is a scalar:

$$F_{ij} = -\frac{\partial^2 \ln \mathcal{L}}{\partial p_i \partial p_j}$$

$$= -\frac{\partial^2 \ln \mathcal{L}}{\partial f_{NL}^2} \delta_{ij} \equiv F,$$
(27)

and the 1σ uncertainty on $f_{\rm NL}$ is

$$\sigma(f_{\rm NL}) = \frac{1}{\sqrt{F}}. (28)$$

The expected noise at a given multipole ℓ is given by

$$\sigma_{\ell}^{2} = \left\langle \left(C_{\ell}^{\mu X} \right)^{2} \right\rangle - \left\langle C_{\ell}^{\mu X} \right\rangle^{2}$$

$$= \frac{C_{\ell}^{\mu \mu} C_{\ell}^{XX} + (C_{\ell}^{\mu X})^{2}}{(2\ell + 1)f_{\text{sky}}},$$
(29)

where $f_{\rm sky}$ is the fraction of the full sky observed in the survey. Our fiducial model for forecasting is $C_\ell^{\mu X}=0$, and we neglect the contribution of the noise part of $C_\ell^{\mu X}$ to the variance, as it will always be much smaller than the product of $C_\ell^{\mu \mu}$ and C_ℓ^{XX} . The likelihood is thus

$$-2 \ln \mathcal{L} = \sum_{\ell=\ell_{\min}}^{\ell_{\max}} (2\ell+1) f_{\text{sky}} \frac{\left(f_{\text{NL}} C_{\ell}^{\mu X} \Big|_{f_{\text{NL}}=1}\right)^{2}}{C_{\ell}^{\mu \mu} C_{\ell}^{XX}}.$$
(30)

For the $C_\ell^{\mu X}$ cross-spectrum (the numerator or signal part of the Fisher matrix calculation), we use the formulation in Eq. (21). For our fiducial forecasts, we adopt $\langle \mu \rangle = 2 \times 10^{-8}$. For the denominator or noise part of the Fisher calculation, we note that the auto-power-spectra C_ℓ^{XX} and $C_\ell^{\mu\mu}$ can be separated into signal and noise terms

$$C_{\ell} = C_{\ell}^S + C_{\ell}^N, \tag{31}$$

where S and N denote signal and noise, respectively. At CMB-S4 noise levels, measurements of both C_{ℓ}^{TT} and C_{ℓ}^{EE} are signal-dominated for $\ell \leq 2000$ (at which point our constraints on $f_{\rm NL}$ are well satu-

rated, see Figure 6). Therefore, we neglect the effects of noise and foregrounds on our temperature and E-mode anisotropy maps, and can make the approximation $C_\ell^{XX} \approx C_\ell^{XX,S}$. On the other hand, measurements of $C_\ell^{\mu\mu}$ will be noise-dominated for the foreseeable future, such that $C_\ell^{\mu\mu} \approx C_\ell^{\mu\mu,N}$. Calculations for $C_\ell^{XX,S}$ are taken from CAMB¹ [55], while $C_\ell^{\mu\mu,N}$ is dependent on instrument and observation parameters, including instrumental and atmospheric noise levels. We describe how we obtain $C_\ell^{\mu\mu,N}$ from noise and foreground models in the following sections.

The constraining power of $C_\ell^{\mu T}$ and $C_\ell^{\mu E}$ for measuring $f_{\rm NL}$ are comparable to each other. Rather than having independent constraints on $f_{\rm NL}$ from $C_\ell^{\mu T}$ or $C_\ell^{\mu E}$, we can use the fact that they both probe the same underlying correlator $\langle \mu \zeta \rangle$ and perform a joint analysis. The authors of Ref. [62] and Ref. [65] demonstrated that the differing behavior of $C_\ell^{\mu T}$ and $C_\ell^{\mu E}$ with ℓ provides a better constraint on $f_{\rm NL}$ than an independent analysis. We follow their method and modify the likelihood function to include the correlations between T and E in both the signal and the covariance. The final likelihood is then

$$-2 \ln \mathcal{L} \approx \sum_{\ell=\ell_{\min}}^{\ell_{\max}} \frac{(2\ell+1)f_{\text{sky}}}{C_{\ell}^{\mu\mu,N} \left[C_{\ell}^{TT} C_{\ell}^{EE} - \left(C_{\ell}^{TE} \right)^{2} \right]} \times (32)$$

$$\left[C_{\ell}^{TT} \left(f_{\text{NL}} C_{\ell}^{\mu E} |_{f_{\text{NL}}=1} \right)^{2} + C_{\ell}^{EE} \left(f_{\text{NL}} C_{\ell}^{\mu T} |_{f_{\text{NL}}=1} \right)^{2} - 2C_{\ell}^{TE} f_{\text{NL}}^{2} C_{\ell}^{\mu T} |_{f_{\text{NL}}=1} C_{\ell}^{\mu E} |_{f_{\text{NL}}=1} \right].$$

B. Component separation

For the purposes of our forecasting, observed maps of the total intensity of the sky in direction \hat{n} and frequency ν_i , $I_i(\hat{n})$, can be described as a linear combination of the CMB μ and T signals and a noise contribution:

$$I_i(\hat{n}) = a_{\mu,i} s_{\mu}(\hat{n}) + a_{T,i} s_{CMB}(\hat{n}) + n_i(\hat{n}),$$
 (33)

where $a_{\mu,i}$ and $a_{\mathrm{T},i}$ are the μ and temperature spectral energy distributions (SEDs) at different frequency bands i, and $s_{\mu}(\hat{n})$ and $s_{\mathrm{CMB}}(\hat{n})$ are the true underlying μ and temperature anisotropy maps. We treat all astrophysical signals that are not CMB μ or T as noise and include them in n. We can choose

 $^{^1}$ http://camb.info

to work in spherical harmonic space, defining $I_{\ell m}$ such that $x(\hat{n}) = \sum_{\ell} \sum_{m} I_{\ell m} Y_{\ell m}(\hat{n})$. We can then rewrite Eq. (33) as

$$I_{\ell m,i} = a_{\mu,i} s_{\ell m,\mu} + a_{T,i} s_{\ell_m,CMB} + n_{\ell m,i}.$$
 (34)

Traditionally, data from CMB experiments are calibrated such that maps in all frequency bands have the same response to primary CMB temperature anisotropy—i.e., the maps are in units of CMB fluctuation temperature ΔT or fractional CMB fluctuation $\Delta T/T$. In the latter case, the CMB temperature SED $a_{\mathrm{T},i}$ is given by

$$a_{\mathrm{T},i} = T_{\mathrm{CMB}} \tag{35}$$

for all bands. We follow Ref. [63] and approximate the μ -distortion SED at frequencies of 20 GHz and above as

$$a_{\mu,i} = T_{\text{CMB}} \left(\frac{1}{2.19} - \frac{1}{x_i} \right),$$
 (36)

where

$$x \equiv \frac{h\nu}{k_{\rm B}T_{\rm CMB}}. (37)$$

We can obtain a temperature-free μ map or its spherical harmonic transform through component separation using a constrained internal linear combination method (CILC) [64]. This method takes advantage of the known SEDs of temperature and μ -distortion anisotropies and calculates weights \boldsymbol{w} that, when applied to observed frequency maps, result in a T-free μ map and a μ -free T map. For example, if we assign the μ weights to the i=0 component of \boldsymbol{w}_{ij} , then the T-free μ map is given by

$$\hat{\mu}_{\ell m}^{T\text{-free}} = \sum_{i} \mathbf{w}_{0i} I_{\ell m,i}$$

$$= 1 * s_{\mu} + 0 * s_{\text{CMB}} + \sum_{i} \mathbf{w}_{0i} n_{\ell m,i}$$
(38)

It is shown in Ref. [63] that the weights that enforce unit response to μ distortions and zero response to temperature anisotropy, and minimize total variance, are given by

$$\boldsymbol{w}^T = \boldsymbol{e}^{t} \left(\mathbf{A}^T \mathbf{C}^{-1} \ \mathbf{A} \right)^{-1} \ \mathbf{A}^T \mathbf{C}^{-1}$$
 (39)

where

$$A = (\boldsymbol{a}_{\mu} \ \boldsymbol{a}_{CMB}) \tag{40}$$

$$\boldsymbol{e}^T = \left(\begin{array}{cc} 1 & 0 \end{array} \right), \tag{41}$$

 $\mathbf{C} = \mathbf{C}_{\ell}^{ij}$ is the frequency-frequency ℓ -space covariance matrix, and T denotes trans-

pose. The above weights can be generalized to null additional components \boldsymbol{b}_m by generalizing A \rightarrow (\boldsymbol{a}_{μ} $\boldsymbol{a}_{\text{CMB}}$ \boldsymbol{b}_1 ... \boldsymbol{b}_m) and $\boldsymbol{e}^T \rightarrow$ (1 0 0 ... 0). We note that the weights depend on multipole number ℓ , i.e., $\boldsymbol{w} \rightarrow \boldsymbol{w}_{\ell}$. For simplicity of notation, we leave the ℓ dependence implicit and continue to use \boldsymbol{w} .

The reduction of the full $\mathbf{C}^{ij}_{\ell m\ell'm'} = \left\langle I^i_{\ell m} I^j_{\ell'm'} \right\rangle$ to \mathbf{C}^{ij}_{ℓ} rests on the assumption that all sources of variance in the maps are isotropic, stationary, and Gaussian. With detector noise only and assuming no correlations between detector noise at different frequencies, the covariance matrix is diagonal $(\mathbf{C}^{ij}_{\ell} = \mathbf{C}^{ii}_{\ell} \delta_{ij})$. Including foregrounds and atmosphere introduces correlated fluctuations between frequency bands and requires the full frequency-frequency matrix.

The assumption of Gaussianity and statistical isotropy is reasonably satisfied by detector noise, atmospheric emission, and extragalactic foregrounds, but not especially well by Galactic foregrounds. The CMB-S4 "ultra-deep" survey, which is the main survey we present forecasts for in this work (see Section IV) is located in an area of the sky with very low Galactic foreground emission. Furthermore, non-Gaussianity in the true foreground emission not accounted for in the covariance will not bias the component separation, it will only make it slightly suboptimal. We note that the Gaussianity of the likelihood (Eq. 33) depends on the power spectrum of the noise sources being Gaussian, not the pixel values or modes of the noise sources themselves, which is a lighter burden owing to the Central Limit Theorem.

We can then obtain $C_\ell^{\mu\mu}$ by applying the μ -distortion weights to the frequency-frequency covariance matrix:

$$C_{\ell}^{\mu\mu} = \sum_{ij} \boldsymbol{w}_{0i} \mathbf{C}_{\ell}^{ij} \boldsymbol{w}_{0j}. \tag{42}$$

We discuss the various contributions to the frequency-frequency covariance matrix \mathbf{C}_{ℓ}^{ij} in the following sections.

C. Instrument noise

Assuming detector noise that is white (uncorrelated between time samples), uniform sky coverage, and a Gaussian instrument beam or point-spread function, the statistics of the map noise for frequency band i in spherical harmonic or ℓ space are given by

$$n_{\ell}^{i} = N^{i} e^{\ell^{2} \theta_{i}^{2} / (16 \ln(2))},$$
 (43)

where N_i and θ_i is are the white noise level in the map and the angular resolution (beam FWHM)

for frequency band i. The contribution to the frequency-frequency covariance matrix from this source will be

$$\mathbf{C}_{\ell}^{ij,N} = \langle n^{i}n^{j} \rangle$$

$$= N^{i}N^{j}e^{\ell^{2}\theta_{i}\theta_{j}/(8\ln(2))}$$

$$(44)$$

and, for detector noise that is uncorrelated between bands,

$$\mathbf{C}_{\ell}^{ij,N} = (N^i)^2 e^{\ell^2 \theta_i^2 / (8 \ln(2))} \delta_{ij}, \tag{45}$$

where δ_{ij} is the Kronecker delta. For white detector noise only, the μ -distortion power spectrum reduces to

$$C_{\ell}^{\mu\mu} = \sum_{i} \boldsymbol{w}_{0i}^{2} (N^{i})^{2} e^{\ell^{2} \theta_{i}^{2} / (8 \ln(2))}. \tag{46}$$

D. Atmosphere

A major source of noise that must be considered in ground-based observations of the CMB is the emission from blobs of poorly mixed water vapor in the Earth's atmosphere (i.e., clouds). For detailed discussions of this effect and measurements of the impact at various sites, see, e.g., Refs. [54], [19], and [58]. The spectrum of cloud sizes is such that the noise power from this source is much larger at large angular scales, and it is often modeled as a power law in ℓ (e.g., Ref. [2]). The total detector + atmosphere noise power in frequency band i can then be parameterized with three numbers, namely the white noise level N_i , the multipole value at which the detector and atmosphere noise levels are equal $\ell_{\text{knee},i}$, and the power-law index of the atmosphere noise $\alpha^{\text{atmo},i}$.

$$\mathbf{C}_{\ell}^{ij,N} = \left[1 + \left(\frac{\ell_{\text{knee},i}}{\ell}\right)^{\alpha^{\text{atmo},i}}\right] (N^i)^2 e^{\ell^2 \theta_i^2 / (8\ln(2))} \delta_{ij}.$$
(47)

Implicit in the formulation of Eq. (47) is the assumption that the atmospheric noise is uncorrelated between bands. In fact, nearly the opposite is the case, at least for detectors for which the beam patterns mostly overlap at the height of the atmospheric emission. For example, internal CMB-S4 analysis of data from the SPT-3G receiver on the South Pole Telescope (SPT, [22, 71]) found that for detectors in different frequency bands but co-located in a focalplane pixel, the long-timescale fluctuations in the time-ordered data were over 99% correlated. To model this, we can introduce an atmospheric correlation parameter η and rewrite the noise + atmosphere contribution to the frequency-frequency covariance

matrix as

$$\mathbf{C}_{\ell}^{ij,N} = \left[1 + \left(\frac{\ell_{\text{knee},i}}{\ell} \right)^{\alpha^{\text{atmo},i}} \right] \times \tag{48}$$

$$(N^{i})^{2} e^{\ell^{2} \theta_{i}^{2}/(8 \ln(2))} \delta_{ij} + \left(\frac{\ell_{\text{knee},i}}{\ell} \right)^{\alpha^{\text{atmo},i}/2} \left(\frac{\ell_{\text{knee},j}}{\ell} \right)^{\alpha^{\text{atmo},j}/2} \times N^{i} N^{j} e^{\ell^{2} \theta_{i} \theta_{j}/(8 \ln(2))} \pi_{ij},$$

where $\pi_{ij} = \eta(1 - \delta_{ij})$. In Sec. V, we will show forecasts using values of using values of η ranging from 0 to 1. As the correlation η increases, the component separation algorithm defined in Sec. III B is more effective in reducing the atmospheric contribution to the final $C_{\ell}^{\mu\mu}$ covariance.

E. Foregrounds

In our forecasting pipeline, we also consider the effects of foregrounds. Foregrounds contribute to the frequency-frequency covariance matrix as linear additions (because they are not correlated with the other sources of covariance) such that

$$\mathbf{C}_{\ell}^{ij} = \mathbf{C}_{\ell}^{ij,N} + \mathbf{C}_{\ell}^{ij,fore} \tag{49}$$

For this work, we approximate all foregrounds as 100% correlated across frequency bands (though we approximate each foreground source as uncorrelated with the others), such that for a given foreground type (call it "type X")

$$\mathbf{C}_{\ell}^{ij,X} = \sqrt{C_{\ell}^{ii,X} C_{\ell}^{jj,X}}.$$
 (50)

Foreground sources can be separated into Galactic and extragalactic sources, and we treat each of these in turn below. Often in the literature, foreground amplitudes and ℓ -space behavior are quoted in $D_{\ell} = \frac{\ell(\ell+1)}{2\pi} C_{\ell}$. When we adopt such parameterizations, we keep the description in D_{ℓ} but convert to C_{ℓ} when actually implementing the model. We show the SEDs of the primary foreground sources, along with the T and μ SEDs, in Figure 2.

1. Galactic Sources

The primary sources of Galactic contamination at CMB observing frequencies are thermal dust emission and synchrotron emission. Interstellar dust heated by starlight emits as a quasi-thermal modified blackbody. We follow Ref. [2] and parameterize the frequency behavior and ℓ -space shape of thermal

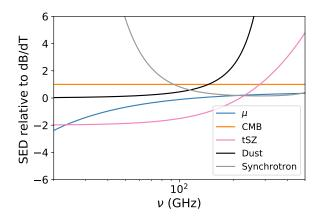


FIG. 2. Spectral shape of CMB anisotropy, μ distortions, and various Galactic and extragalactic foregrounds, all divided by the CMB anisotropy SED and scaled by an arbitrary amplitude. For frequencies $\nu < 100\,\mathrm{GHz}$, we see that Galactic synchrotron sharply rises, even relative to μ distortions. At frequencies $\nu > 100\,\mathrm{GHz}$, Galactic dust and the thermal SZ effect start growing as the μ -distortion spectrum starts leveling off.

dust emission as

$$D_{\ell,\nu_{1},\nu_{2}}^{d} = D_{80,\nu_{0}}^{d} \epsilon_{\nu_{1},\nu_{2}} \left(\frac{\nu_{1}\nu_{2}}{\nu_{0}^{2}}\right)^{\alpha^{d}} \times \frac{B_{\nu_{1}} (T_{d}) B_{\nu_{2}} (T_{d})}{B_{\nu_{0}}^{2} (T_{d})} \left(\frac{\ell}{80}\right)^{-0.4},$$
(51)

where B is Planck's law, $D_{80,\nu_0}^{\rm d}$ is the value of D at $\ell=80$ and the reference frequency ν_0 , $T_{\rm d}$ is the dust temperature, and $\alpha^{\rm d}$ is the dust spectral index. Following Ref. [38], we define $D_{80}^{\rm d}=3.253\,\mu{\rm K}^2,\,\alpha^{\rm d}=1.6,\,T_{\rm d}=19.6,\,{\rm and}\,\,\nu_0=145\,{\rm GHz}.\,$ Finally, ϵ_{ν_1,ν_2} relates the brightness of CMB fluctuations at $\nu_1,\,\nu_2,\,{\rm and}\,\,\nu_0$:

$$\epsilon_{\nu_1,\nu_2} \equiv \frac{\left[\frac{dB(\nu_0, T_{\text{CMB}})}{dT}\right]^2}{\frac{dB(\nu_1, T_{\text{CMB}})}{dT} \frac{dB(\nu_2, T_{\text{CMB}})}{dT}}.$$
 (52)

Because we have defined our μ and T SEDs assuming that the input maps are calibrated to CMB fluctuation amplitudes, we must also account for this in the foreground modeling. The ratio $1/(dB/dT|_{\nu,T_{\rm CMB}})$ converts the source radiance of a given foreground at frequency ν to an equivalent CMB temperature anisotropy.

We use a similar parameterization for Galactic synchrotron, again following Ref. [2]

$$D_{\ell,\nu_1,\nu_2}^{\text{sync}} = D_{80,\nu_0}^{\text{sync}} \epsilon_{\nu_1,\nu_2} \left(\frac{\nu_1 \nu_2}{\nu_0^2}\right)^{\alpha^{\text{sync}}} \left(\frac{\ell}{80}\right)^{-0.4} (53)$$

and we again adopt values from Ref. [38]: $D_{80}^{\rm sync}=$

 $0.005 \,\mu\mathrm{K}^2$, $\alpha^\mathrm{sync} = -1.10$, and $\nu_0 = 93 \,\mathrm{GHz}$. We note that both the synchrotron and dust amplitudes used here are estimated for the CMB-S4 "ultradeep" $f_\mathrm{sky} = 0.03$ survey (see next section for details).

Because of the shape of the μ -distortion SED, lower-frequency channels are particularly important for recovering the signal, and it is possible that other Galactic foregrounds such as free-free emission and "anomalous microwave emission" (AME) could be important contaminants. We investigate the behavior of these additional foregrounds in the CMB-S4 3% sky region using PySM [75], which is based on the Planck Sky Model [37]. We find that the AME SED has a double-peaked shape, which we parameterize as

$$f_{\text{AME}}^{2}(\nu) = \frac{e^{-[\ln(\nu) - \ln(\nu_{a1})]^{2}/2\sigma_{a1}^{2}} + Ae^{-[\ln(\nu) - \ln(\nu_{a2})]^{2}/2\sigma_{a2}^{2}}}{1 + Ae^{-[\ln(\nu_{a1}) - \ln(\nu_{a2})]^{2}/2\sigma_{a1}^{2}}},$$
(54)

with $\nu_{a1}=10\,\mathrm{GHz}$, $\sigma_{a1}=0.43\,\mathrm{GHz}$, $\nu_{a2}=22\,\mathrm{GHz}$, $\sigma_{a2}=0.35\,\mathrm{GHz}$, and A=0.0065. We assume similar ℓ -space behavior as the thermal dust and write

$$D_{\ell,\nu_1,\nu_2}^{\text{AME}} = D_{80,\nu_0}^{\text{AME}} f_{\text{AME}}(\nu_1) f_{\text{AME}}(\nu_2) \left(\frac{\ell}{80}\right)^{-0.4},$$
(55)

with $D_{80,\nu_0}^{\rm AME}=1.0\times10^4\mu{\rm K}^2$ at $\nu_0=10\,{\rm GHz}$. The free-free emission in the CMB-S4 3% sky region appears to be dominated by point-like sources (either residual contributions from extragalactic radio sources or emission from compact HII regions). Because CMB-S4 will have the sensitivity and resolution to find and mask such sources, we neglect the contribution of free-free emission in this analysis.

2. Extragalactic foregrounds

In addition to emission from our Galaxy, we also need to consider foreground emission from extragalactic sources. We treat four independent types of extragalactic foregrounds: the thermal Sunyaev-Zel'dovich (tSZ) effect, the clustered cosmic infrared background (CIB), the unclustered ("shot-noise" or "Poisson") component of the CIB, and synchrotron-emitting active galactic nuclei (or "radio sources"), the clustering of which is assumed to be negligible. We neglect the contribution from the kinetic Sunyaev-Zel'dovich (kSZ) effect, which has the same frequency spectrum as the CMB and will be nulled by the CILC.

The tSZ effect, a type of y distortion, arises from CMB photons scattering off electrons in the intracluster medium of galaxy clusters and other collapsed structures. This shifts the re-emitted photons to higher frequencies compared to the CMB spectrum. We parameterize the tSZ as

$$D_{\ell,\nu_1,\nu_2}^{\text{tSZ}} = D_{3000,\nu_0}^{\text{tSZ}} T(\ell) \frac{f(\nu_1)f(\nu_2)}{f^2(\nu_0)}, \quad (56)$$

where

$$f(\nu) = x \frac{e^x + 1}{e^x - 1} - 4,\tag{57}$$

$$x = \frac{h\nu}{k_{\rm B}T},\tag{58}$$

and $T(\ell)$ is the tSZ template used in Ref. [72]. Following Ref. [43], we adopt $D_{3000,\nu_0}^{\rm tSZ}=3.4\,\mu{\rm K}^2$ at $\nu_0=150\,{\rm GHz}$.

Again following Ref. [43], we parameterize the clustered CIB as

$$D_{\ell,\nu_1,\nu_2}^{c} = D_{3000}^{c}(\nu_0)\epsilon_{\nu_1,\nu_2} \left(\frac{\nu_1\nu_2}{\nu_0^2}\right)^{\alpha^p} \left(\frac{\ell}{3000}\right)^{0.8} (59)$$

where $D_{3000}^{\rm c}(\nu_0) = 3.46 \mu {\rm K}^2$, $\alpha^{\rm p} = 4.27$, and $\nu_0 = 150 \, {\rm GHz}$. And we parameterize the Poisson component of the CIB as

$$D_{\ell,\nu_1,\nu_2}^{\rm p} = D_{3000}^{\rm p}(\nu_0)\epsilon_{\nu_1,\nu_2} \left(\frac{\nu_1\nu_2}{\nu_0^2}\right)^{\alpha^{\rm p}} \left(\frac{\ell}{3000}\right)^2 (60)$$

with $D_{3000}^{\rm p} = 9.16 \mu {\rm K}^2$, $\alpha^{\rm p} = 3.27$, $\nu_0 = 150 \, {\rm GHz}$. For this initial work, we do not consider spatial correlation between the tSZ and CIB. This does not cause any direct bias to our final result, as we explicitly null any signal with a tSZ spectrum in our final constraints (see Section V for details). For more discussion of the effects of tSZ-CIB correlation on $\mu \times T$ measurements, see Ref. [66].

Finally, we parameterize radio source power as

$$D_{\ell,\nu_1,\nu_2}^{\rm r} = D_{3000}^{\rm r}(\nu_0)\epsilon_{\nu_1,\nu_2} \left(\frac{\nu_1\nu_2}{\nu_0^2}\right)^{\alpha^{\rm p}} \left(\frac{\ell}{3000}\right)^2 (61)$$

with $D_{3000}^{\rm r}(\nu_0)=0.02\,\mu{\rm K}^2,~\alpha^{\rm p}=-0.7,~\nu_0=150\,{\rm GHz}.$ This is significantly lower than amplitudes quoted in, e.g., Ref. [43]. This is because the radio Poisson power is dominated by the brightest individual sources in the map, and masking and removing the brightest radio sources will reduce the Poisson term. For an experiment similar to CMB-S4, which will achieve roughly 1 $\mu{\rm K}$ -arcmin map noise, radio sources can be cleaned down to roughly $0.2\,{\rm mJy},$ which reduces their Poisson amplitude to $D_{3000}^{\rm r}(\nu_0)=0.02\,\mu{\rm K}^2.$

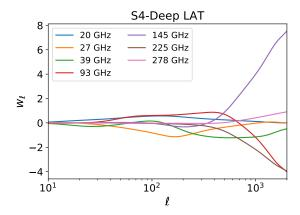
F. Calibration

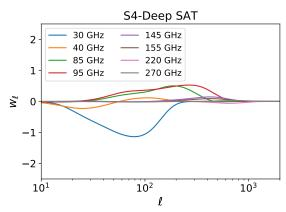
Historically, measurements of absolute brightness or temperature at microwave/millimeter-wave frequencies have been successfully carried out only by space- or balloon-borne telescopes, because of the stringent requirements on calibration accuracy and stability (e.g., Refs. [51, 57]). Proposed measurements of the absolute μ -distortion amplitude, such as with the PIXIE satellite [52], are designed with similar constraints in mind. It was pointed out, however, in Ref. [42] that measuring the anisotropy of μ distortions, and particularly the correlated anisotropy of μ and temperature, effectively converts the absolute calibration requirement to a relative calibration requirement, and the bias on the absolute measurement to an uncertainty on the measurement of anisotropy.

A calibration error in CMB-S4-like data will result primarily in leakage of the much larger temperature signal (or foregrounds) into the componentseparated μ map, resulting in a component of $T \times T$ in the $\mu \times T$ cross-spectrum. The $T \times T$ spectrum does not have the same shape as $\mu \times T$ (which crosses zero many times over the ℓ range we consider), so there will be on average no bias from this leakage, just excess variance. We have investigated the level to which the relative calibration must be known for this variance not to dominate the error on $f_{\rm NL}$, but a simple scaling argument tells us that, because the relative calibration will come from enforcing equal response to the CMB temperature in every frequency band, the calibration precision in any one band will be equal to the S/N on the CMB temperature anisotropy in that band. Thus, the contribution to uncertainty on $f_{\rm NL}$ from calibration errors will be on the order of the contribution from noise divided by the square root of the number of bands. For this reason, we ignore calibration uncertainty in our main results.

A related concern is the knowledge of the instrumental bandpasses. Even in the limit of perfect relative calibration off the CMB, imperfect knowledge of the instrument bandpasses could lead to a different level of foreground contamination in the μ map than the component-separation algorithm predicts. As with CMB T leakage, this will not generally have the same shape as the $\mu \times T$ spectrum and will thus not cause bias on average. Furthermore, as we are not explicitly projecting out foregrounds in the component separation, the extra leakage of foregrounds into the μ map from bandpass uncertainty is likely to be small. Nevertheless, we will update the forecasting machinery to include this effect in a future paper.

IV. SURVEY CONFIGURATION





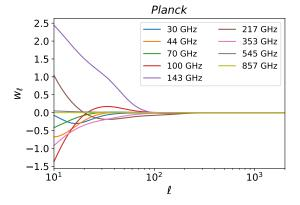


FIG. 3. Weights used to construct the T-free μ -distortion map (i.e., the μ component of \boldsymbol{w}) for the CMB-S4 ultradeep patch from different frequency channels, including foregrounds and assuming 99% correlated atmosphere.

In this work, we are forecasting $\sigma(f_{\rm NL})$ using the parameters of the upcoming CMB-S4 experiment [1]. There are two major surveys planned for CMB-S4, an "ultra-deep" survey of roughly 3% of the Southern sky, conducted from the South Pole with both small-aperture telescopes (SATs) and a large-

aperture telescope (LAT), and a "deep and wide" survey of roughly 60% of the sky, conducted from Chile with LATs only.

Our fiducial forecasting will be for the $f_{\rm sky}=0.03$ survey. The $f_{\rm sky}=0.6$ survey involves a similar investment of total detector number and observing time, but spread across a sky patch that is 20 times larger. In the limit of detector noise only, this introduces a factor $f_{\rm sky}$ into the covariance matrix, leading to

$$\mathbf{C}_{\ell}^{ij,N}(f_{sky}) = \mathbf{C}_{\ell}^{ij,N}(f_{sky} = 0.03) \frac{f_{sky}}{0.03}.$$
 (62)

Because incomplete sky surveys also observe fewer total sky modes and hence have fewer samples of the various power spectra, the Fisher matrix calculations also include an $f_{\rm sky}$ term, as in Eq. (29).

As discussed in the previous section, we can make the approximation that $C_\ell^{\mu\mu}$ is noise-dominated, while C_ℓ^{TT} is signal-dominated for $\ell \leq 2000$. This means that $C_\ell^{\mu\mu}$ is the only term in the denominator of the $\mu \times T$ Fisher calculation that has an $f_{\rm sky}$ dependence:

$$-2 \ln \mathcal{L} = \sum_{\ell=2}^{\ell_{\text{max}}} 0.03 \ (2\ell+1) \frac{f_{\text{sky}}}{0.03} \times$$

$$\frac{\left(f_{\text{NL}} C_{\ell}^{\mu T} \Big|_{f_{\text{NL}}} \right)^{2}}{(f_{\text{sky}}/0.03) \ C_{\ell}^{\mu\mu,\text{N}}|_{f_{\text{sky}}=0.03} \ C_{\ell}^{TT}}.$$

$$(63)$$

In this limit, $f_{\rm sky}$ cancels out, leaving our Fisher matrix independent of $f_{\rm sky}$ in the detector-noise-only case. We note that this will be true for any measurement that depends on correlating a very small signal (that is below the detection threshold for a given experiment) with a much larger one (that is measured at high S/N).² When we add atmosphere and foregrounds, the situation becomes more complicated, because the statistics of the atmospheric noise are different at the two CMB-S4 sites, and because it is more difficult to avoid bright parts of our Galaxy when more sky is observed.

The parameters of the high-resolution (LAT) part of the ultra-deep ($f_{\rm sky}=0.03$) survey, including band centers, angular resolutions, and noise levels, are given in Table I. The corresponding values for the degree-scale (SAT) ultra-deep survey are shown in Table II.

The $f_{\rm sky}=0.03$ ultra-deep survey for CMB-S4 will be conducted from the South Pole. In terms of

One caveat to this is that the survey needs to be big enough to resolve the largest scale that is important for measuring the signal.

Frequency (GHz)	20	27	39	93	145	225	278
Angular resolution (arcmin)	11	8.4	5.8	2.5	1.6	1.1	1.0
White noise level in temperature (μ K-arcmin)	9.31	4.6	2.94	0.45	0.41	1.29	3.07
$\ell_{\rm knee}$ for TT	400	400	400	1200	1900	2100	2100
α for TT	4.2	4.2	4.2	4.2	4.1	4.1	3.9

TABLE I. Survey configuration for the large-aperture telescope (LAT) in the CMB-S4 ultra-deep survey.

Frequency (GHz)	30	40	85	95	145	155	220	270
Angular resolution (arcmin)	72.8	72.8	25.5	22.7	25.5	22.7	13.0	13.0
White noise level in polarization (μ K-arcmin)	3.53	4.46	0.88	0.78	1.23	1.34	3.48	5.97
White noise level in temperature (μ K-arcmin)	2.50	3.15	0.62	0.55	0.87	0.95	2.46	4.22
ℓ_{knee} for TT	400	400	1200	1200	1900	1900	2100	2100
α for TT	4.2	4.2	4.2	4.2	4.1	4.1	4.1	3.9

TABLE II. Survey configuration for the small-aperture telescopes (SATs) in the CMB-S4 ultra-deep survey.

atmospheric emission at CMB frequencies, the South Pole is the best large, developed site on Earth [53]. In Tables I and II, we show the expected values of $\ell_{\rm knee}$ and α (see Eq. 47) for the CMB-S4 bands at the South Pole, derived from CMB-S4 internal analysis of SPT-3G data. We note that the Deep Survey LAT value for $\ell_{\rm knee}$ for bands below 40 GHz in official CMB-S4 documents is 1200, while we use 400 here. The value of 1200 is a conservative choice made assuming no improvement in atmospheric noise from the lowest SPT band of 95 GHz. The $\ell_{\rm knee}$ values for the Wide Survey LAT low-frequency bands, which were derived by scaling the atmospheric noise power with levels of precipitable water vapor, are close to 400, and thus we adopt that value for the Deep Survey here. We discuss the impact of this choice in Section V.

In addition to reducing raw noise levels, the authors of Ref. [63] suggest expanding detector frequency coverage, in order to lower $C^{\mu\mu,N}$. To increase the upper frequency range of CMB-S4 measurements, we include Planck 2018 data in the forecast, which extends up to 857 GHz. This should provide valuable complementary information that can help mitigate foregrounds at frequencies that CMB-S4 is unable to observe. We implement *Planck* bands in our forecasting pipeline in the same way as CMB-S4 (as independent frequency channels, over the same 3% of the sky as CMB-S4 Deep), using the parameters shown in Table III. In Figure 3, we show the components of \boldsymbol{w} for the T-free μ map contributed from each individual CMB-S4 or *Planck* band, assuming 99% atmospheric correlation and the foregrounds described in the previous section.

In Figure 4, we show the expected noise power in the μ map from CMB-S4 $(C_\ell^{\mu\mu,N})$ for various values of atmospheric correlation among frequency bands. In the scenario where frequency bands are fully correlated and the atmosphere can be fully subtracted out, the associated noise curve closely matches the scenario with no atmosphere. However, even minimal decorrelation among detectors significantly worsens $C_\ell^{\mu\mu,N}$ at low multipoles. Residual atmosphere acts as an effective ℓ_{\min} when summing over multiple observation bands to constrain f_{NL} .

We note that currently fielded experiments such as Advanced ACTPol [44] and SPT-3G, as well as the upcoming Simons Observatory (SO) experiment [6] can be approximated in this forecasting framework as versions of either the CMB-S4 Deep or Wide surveys, but with higher noise and (in the case of currently fielded experiments) reduced frequency coverage. In particular, the SO LAT "goal" survey is similar to the CMB-S4 Wide survey with 2-3 times higher noise and slightly less sky area, thus we would thus expect to forecast roughly 2-3 times worse constraints on $f_{\rm NL}$ for SO compared to CMB-S4.

V. RESULTS

Using the noise, atmosphere, and foreground paramaterizations described in the previous sections, we forecast $\sigma(f_{\rm NL})$ from the combination of $\mu \times T$ and $\mu \times E$ for the CMB-S4 experiment, combined with data from the *Planck* satellite [7]. For our results,

Frequency (GHz)	30	44	70	100	143	217	353	545	857
Angular resolution (arcmin)	32.4	27.1	13.3	9.69	7.30	5.02	4.94	4.83	4.64
White noise level for TT (μ K-arcmin)	150	162	210	77.4	33.0	46.8	154	815	2.98×10^4

TABLE III. Angular resolution and noise levels assumed for *Planck* (reproduced from Table 4 of Ref. [7]). Note that we assume *Planck* noise is white down to the ℓ_{\min} of our forecasting.

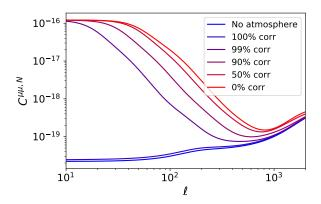


FIG. 4. $C_\ell^{\mu\mu,N}$ for the CMB-S4 ultra-deep survey and various assumptions for the degree of atmospheric correlation between bands. Full correlation among bands closely matches the nominal case of no atmosphere. However, even minimal decorrelation among detectors significantly worsens $C_\ell^{\mu\mu,N}$ at low multipoles.

we assume a fiducial value of $f_{\rm NL}=1$. We will generally show the cumulative constraint on $f_{\rm NL}$ as a function of $\ell_{\rm max}$, the highest multipole value considered in the calculation. In all cases, we assume $\ell_{\rm min}=10$, though our final results are not sensitive to this exact choice.

We first show, in Figure 5, the signal-to-noise (S/N) as a function of multipole ℓ . The solid lines include detector and atmospheric noise and foreground residual, with color differentiating the amount of assumed atmospheric correlation between frequency bands. The dashed lines correspond to detector and atmospheric noise only, with no foreground residuals.

For the scenario where atmosphere is perfectly correlated between frequency bands we see that most of our signal is at the lowest ℓ modes. The addition of foregrounds reduces our overall signal by about an order of magnitude, agreeing with previous results [63] that foregrounds are a primary obstacle for experiments constraining μ distortions.

The main foregrounds that impact our constraints are from Galactic sources, such as dust, synchrotron radiation, and AME. Galactic foregrounds have a larger effect on reducing sensitivities to μ , compared to extragalactic sources [65]. Even though several

Galactic and extragalactic foregrounds are brighter at lower frequencies, the shape of the μ SED becomes more distinct for these frequency bands. This suggests for optimal detection of μ distortions, future experiments should concentrate on improving observations with lower frequency bands rather than higher frequency ones. In spite of foreground residuals, in the limit of 100% atmospheric correlation between bands, we find that the lowest ℓ modes provide the best leverage for constraining $f_{\rm NL}$.

However, when we introduce any atmospheric decorrelation, residual atmosphere has a more significant impact on our μ maps than residual foregrounds. While foregrounds reduce the S/N across the entire ℓ range, atmosphere suppresses the S/N primarily at low ℓ , where the raw S/N is highest. This means that we lose significant leverage in constraining $f_{\rm NL}$ from atmospheric contamination.

Another potential contamination to measurements of $\mu \times T$ correlations are y-type spectral distortions. In our default component-separation algorithm, y distortions are treated as noise and not explicitly projected out of the μ or T map. However, the authors of Ref. [62] showed that there are $y \times T$ correlations induced from late Integrated Sachs-Wolfe effects. This means that $y \times T$ correlations will leak into our $\mu \times T$ correlations and potentially bias $\sigma(f_{\rm NL})$, unless we deproject them explicitly. This is easily accomplished in the algorithm by adding the y-distortion SED as one of the components in the matrix A in Eq. (39), but we pay some noise penalty for this.

Figure 6 shows our constraints on $f_{\rm NL}$ (including projecting out a y component) after summing over all multipoles up to $\ell_{\rm max}$. We consider different values of atmospheric correlation and the presence of foregrounds. We see that at $\ell_{\rm max}=2000$, we have effectively saturated our constraints on $f_{\rm NL}$ for all configurations. Therefore, in Tables IV and V, we report $\sigma(f_{\rm NL})$ for $\ell_{\rm max}=2000$.

In the ideal case in which we can ignore atmosphere, foregrounds, and y distortions, we find $\sigma(f_{\rm NL})=48$. The addition of foregrounds worsens our constraints to $\sigma(f_{\rm NL})=475$, or 477 if we project out y. This is better than forecasts for Lite-BIRD, which is forecasted to achieve $\sigma(f_{\rm NL})=825$ [65]. Adding atmosphere and assuming some level

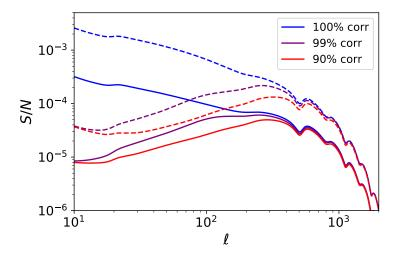


FIG. 5. Signal-to-noise (S/N) per multipole for various assumed values of atmospheric correlation between bands. Dashed lines correspond to S/N when only including instrumental and atmospheric noise, while solid lines also include the effects of foregrounds.

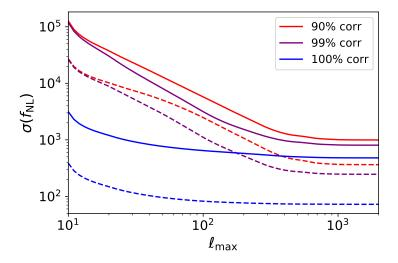


FIG. 6. 1- σ constraints on $f_{\rm NL}$ as a function of the maximum multipole used in analysis, $\ell_{\rm max}$. Dashed lines correspond to $\sigma(f_{\rm NL})$ when only including instrumental and atmospheric noise, while solid lines also include the effects of foregrounds. In all cases, the y SED has been projected out (see text for details).

of decorrelation across frequency bands, we find our constraints on $f_{\rm NL}$ noticeably degrade even in the absence of foregrounds. For 1% decorrelation $(\eta=99\%)$ we find $\sigma(f_{\rm NL})=176$, or 246 with projecting out y. The addition of foregrounds further reduces constraints, with $\sigma(f_{\rm NL})=793$ or 804 in the case of 1% atmospheric decorrelation, comparable to the forecast for LiteBIRD. We note that, because of the effect of atmosphere on CMB-S4 constraints and the low angular resolution of LiteBIRD, it is likely that the $f_{\rm NL}$ constraints from the two experiments will come primarily from independent regions of ℓ

space, in which case we will be able to improve the individual constraints by nearly a factor of $\sqrt{2}$ by combining them.

Foreground residuals can in principle be reduced through expanded frequency coverage. If the foreground SEDs are smooth and require minimal degrees of freedom to model, with enough observations across unique frequency bands, one can constrain the foreground and CMB SEDs. Pairing CMB-S4 with additional surveys that aim to accurately model CMB foregrounds can greatly improve our constraints on $f_{\rm NL}$. However, even with reduced

$\sigma(f_{ m NL}),$	S4-Deep + Planck	$S4 ext{-}Deep + Planck$
$\ell_{\rm max} = 2000$	(no foregrounds)	
No atmosphere	48	475
100% correlated	55	478
99% correlated	176	793
90% correlated	258	963
70% correlated	324	1107

TABLE IV. Constraints on $f_{\rm NL}$ from the CMB-S4 ultra-deep survey and Planck, considering the effects of atmosphere and foregrounds. In the case where neither are present, $\sigma(f_{\rm NL}) = 48$. Including atmosphere and foregrounds worsens this constraint by at least an order of magnitude.

$\sigma(f_{\rm NL})$, "null-y"	$S4 ext{-}Deep + Planck$	S4-Deep + Planck
$\ell_{\rm max} = 2000$	(no foregrounds)	
No atmosphere	68	477
100% correlated	72	479
99% correlated	246	804
90% correlated	364	995
70% correlated	458	1162

TABLE V. Constraints on $f_{\rm NL}$ when projecting out the y SED, from the CMB-S4 ultra-deep survey and *Planck*. We see in the case of no foregrounds that constraints on $f_{\rm NL}$ are worse than the ones given in Table IV. Including foregrounds, we see that constraints are very similar to those obtained if we did not project out the y SED.

foreground residuals, CMB-S4 will be limited by atmospheric noise to $\sigma(f_{\rm NL}) > 100$, unless the correlation between bands is > 99%.

VI. DISCUSSION

In this work, we have presented forecasted constraints on $f_{\rm NL}$, at effective scales of $k \simeq 740\,{\rm Mpc}^{-1}$, with CMB-S4 using correlations of μ -distortion anisotropies with CMB temperature and E-mode polarization. We find that with this ground-based experiment we are able to achieve comparable results to forecasts for the LiteBIRD satellite [65], depending on the amount of atmospheric correlation among frequency bands. CMB-S4 will not have prior knowledge of the amount of atmospheric correlation, which is expected to depend on the optical design and observing strategy. Co-located detectors will likely be more correlated, since they will observe along the same incident angle and will observe similar parts of the atmosphere. Conversely, detectors located further from each other will observe through slightly different columns of the atmosphere and are expected to be less correlated. Understanding the correlation properties of atmospheric emission between frequency bands is therefore vital for producing realistic forecasts of $\sigma(f_{\rm NL})$ from μ -distortion anistropies.

Independent of the details of atmospheric correlation, we have demonstrated that CMB-S4 has the potential to constrain small-scale Gaussianities down to $\sigma(f_{\rm NL}) \lesssim 1000$ with $\mu \times T$ and $\mu \times E$. We note that correlations between μ -distortion and primary CMB anisotropies represent one of our only probes for understanding non-Gaussianities on extremely small scales or, equivalently, the ultrasqueezed-limit of the bispectrum. This presents an opportunity to constrain inflationary models that predict specific behavior at very small scales. One such area that can be constrained with small-scale non-Gaussianities are inflationary models that contain additional fields. Certain curvaton models can naturally generate $f_{\rm NL} \gg 1$ on small scales while preserving current upper limits on $f_{\rm NL}(0.05~{\rm Mpc^{-1}})$ from Planck [39]. If massive fields have direct couplings to the inflaton, they can also induce oscillatory features in the squeezed-limit bispectrum at small scales [13]. Modified (non-Bunch-Davies) initial vacuum states can also produce enhanced smallscale non-Gaussianity [42] and can be constrained with $\mu \times T$ and $\mu \times E$ correlations. Finally, $\mu \times T$ and $\mu \times E$ correlations can place stringent constraints on the running of the spectral index $n_{\rm s}$ and general scale-dependent non-Gaussianities [41], such as have been proposed to explain recent discoveries from the James Webb Space Telescope [16].

It is also worth noting that the constraint on $f_{\rm NL}$ from $\mu \times T$ and $\mu \times E$ is linearly proportional to the mean value of μ (cf. Eqs. 28 and 21), so any nonstandard model that boosts $\langle \mu \rangle$ will correspondingly improve the forecasted constraints on $f_{\rm NL}[29]$. One example of such a model is given in Ref. [60], in which the authors used $\mu \times T$ to constrain primordial black hole (PBH) models. PBH models generically have a rising slope for the power spectrum at small scales, preceded by a region with lower power. For scales close to the ones μ distortions. probe, the rising power can enhance $\langle \mu \rangle$, while the dip can generate non-Gaussianities larger than slow-roll predictions. These combined effects mean that upcoming CMB experiments can potentially rule out some PBH models. Work in Ref. [79] has shown that the main signal PBH models imprint on $\mu \times T$ is from local modulation of acoustic dissipation by long wavelength modes, which induce a bias in μ distortions. We will examine this potential signal in future work.

Our analysis probes non-Gaussianities from scalar perturbations $\langle \zeta \zeta \zeta \rangle$. Distortions of the μ type should also be generated by primordial gravitational waves (GW) injecting energy into the photon-baryon fluid. This allows μ to probe the primordial tensor power spectrum. Since gravitational waves are free streaming throughout the radiation-dominated era, tensor $\mu^{(t)}$ -distortions probe scales in the range $1\,\mathrm{Mpc}^{-1} \lesssim k \lesssim 10^6\,\mathrm{Mpc}^{-1}$, complementing the gap between CMB scales and the scales probed by upcoming GW interferometers [50]. Recent work in Ref. [59] has demonstrated that $\mu \times B$ correlations can probe tensor and mixed tensor-scalar non-Gaussianities. Using FIRAS data, Ref. [17] attempted the first measurement of $\mu \times B$, which they found was consistent with zero at existing noise levels.

The forecasts presented here are not the last word on $f_{\rm NL}$ from $\mu \times T$ and $\mu \times E$. As shown in Ref. [21], a cosmic-variance limited experiment can in principle constrain $\sigma(f_{\rm NL})$ to $\lesssim 10^{-3}$ with $\mu \times T$, although this will also require a significantly improved limit on the average μ -distortion amplitude to break

the degeneracy between $f_{\rm NL}$ and $\langle \mu \rangle$ [29] and ensure that no other source of distortion anisotropies is present [32]. Putting this in context, the best constraints a cosmic-variance limited CMB experiment could place on squeezed-limit non-Gaussianity with $\langle TTT \rangle$ is $\sigma(f_{\rm NL}) \sim 1$. One promising avenue for improvement on the constraints presented here is suggested in Ref. [63], namely expanding coverage to lower frequency ranges where the relative amplitude of the μ -distortion SED is higher. In particular, the addition of bands at and below 10 GHz would significantly improve detection. One possibility is to combine CMB-S4 with upcoming low-frequency radio surveys such as the Square Kilometer Array (SKA) [77] to improve constraints on $f_{\rm NL}$, an aspect we will explore in future work.

ACKNOWLEDGMENTS

T.C. and D.Z. acknowledge support from NSF award OPP-1852617. D.Z. was additionally supported by the National Science Foundation (NSF) Graduate Research Fellowship Program under Grant No. DGE1746045 and the University of Chicago McCormick Fellowship. J.C. was supported by the Royal Society as a Royal Society University Research Fellow at the University of Manchester, UK (No. URF/R/191023) and by the ERC Consolidator Grant CMBSPEC (No. 725456). G.F. acknowledges the support of the European Research Council under the Marie Skłodowska Curie Actions through the Individual Global Fellowship No. 892401 PiCOGAMBAS. D.G. acknowledges support in part by NASA ATP Grant No. 17-ATP17-0162, NSF PHY-2112846, and the provost's office of Haverford College. V.G. acknowledges the support from NASA through the Astrophysics Theory Program, Award Number 21-ATP21-0135 and from the National Science Foundation under Grant No. PHY-2013951. J.C.H. acknowledges support from NSF grant AST-2108536, NASA grant 21-ATP21-0129, DOE grant DE-SC00233966, the Sloan Foundation, and the Simons Foundation. P.D.M. and G.O. acknowledge support from the Netherlands organization for scientific research (NWO) VIDI grant (dossier 639.042.730). M.R. thanks the Spanish Agencia Estatal de Investigacion (AEI, MICIU) for the financial support provided under the project with reference PID2019-110610RB-C21.

^[1] Kevork Abazajian et al. CMB-S4 Science Case, Reference Design, and Project Plan. 7 2019.

^[2] Kevork Abazajian et al. CMB-S4: Forecasting Constraints on Primordial Gravitational Waves. 8 2020.

- [3] Kevork N. Abazajian et al. CMB-S4 Science Book, First Edition. 10 2016.
- [4] Ana Achucarro, Jinn-Ouk Gong, Sjoerd Hardeman, Gonzalo A. Palma, and Subodh P. Patil. Features of heavy physics in the CMB power spectrum. *JCAP*, 01:030, 2011.
- [5] P. A. R. Ade et al. Improved Constraints on Primordial Gravitational Waves using Planck, WMAP, and BICEP/Keck Observations through the 2018 Observing Season. *Phys. Rev. Lett.*, 127(15):151301, 2021
- [6] Peter Ade et al. The Simons Observatory: Science goals and forecasts. *JCAP*, 02:056, 2019.
- [7] N. Aghanim et al. Planck 2018 results. I. Overview and the cosmological legacy of Planck. Astron. Astrophys., 641:A1, 2020.
- [8] N. Aghanim et al. Planck 2018 results. VI. Cosmological parameters. Astron. Astrophys., 641:A6, 2020. [Erratum: Astron. Astrophys. 652, C4 (2021)].
- [9] Y. Akrami et al. Planck 2018 results. IX. Constraints on primordial non-Gaussianity. Astron. Astrophys., 641:A9, 2020.
- [10] Mohsen Alishahiha, Eva Silverstein, and David Tong. DBI in the sky. Phys. Rev. D, 70:123505, 2004.
- [11] James Annis, Jeffrey A. Newman, and Anže Slosar. Snowmass2021 Cosmic Frontier: Report of the CF04 Topical Group on Dark Energy and Cosmic Acceleration in the Modern Universe. 9 2022.
- [12] Nima Arkani-Hamed, Paolo Creminelli, Shinji Mukohyama, and Matias Zaldarriaga. Ghost inflation. JCAP, 04:001, 2004.
- [13] Nima Arkani-Hamed and Juan Maldacena. Cosmological Collider Physics. 3 2015.
- [14] Neil Barnaby and Sarah Shandera. Feeding your Inflaton: Non-Gaussian Signatures of Interaction Structure. JCAP, 01:034, 2012.
- [15] Daniel Baumann and Daniel Green. Signatures of Supersymmetry from the Early Universe. Phys. Rev. D, 85:103520, 2012.
- [16] M. Biagetti, G. Franciolini, and A. Riotto. The JWST High Redshift Observations and Primordial Non-Gaussianity. 10 2022.
- [17] Federico Bianchini and Giulio Fabbian. CMB spectral distortions revisited: A new take on μ distortions and primordial non-Gaussianities from FIRAS data. *Phys. Rev. D*, 106(6):063527, 2022.
- [18] Carlo Burigana, L. Danese, and G. De Zotti. Formation and evolution of early distortions of the microwave background spectrum A numerical study. Astron. Astrophys., 246(1):49–58, 1991.
- [19] Robert S. Bussmann, W. L. Holzapfel, and C. L. Kuo. Millimeter wavelength brightness fluctuations of the atmosphere above the South Pole. Astrophys. J., 622:1343–1355, 2005.
- [20] Giovanni Cabass, Alessandro Melchiorri, and Enrico Pajer. μ distortions or running: A guaranteed discovery from CMB spectrometry. *Phys. Rev. D*, 93(8):083515, 2016.
- [21] Giovanni Cabass, Enrico Pajer, and Drian van der Woude. Spectral distortion anisotropies from single-

- field inflation. JCAP, 08:050, 2018.
- [22] J. E. Carlstrom et al. The 10 Meter South Pole Telescope. Publ. Astron. Soc. Pac., 123:568–581, 2011.
- [23] Xingang Chen, Min-xin Huang, Shamit Kachru, and Gary Shiu. Observational signatures and non-Gaussianities of general single field inflation. JCAP, 01:002, 2007.
- [24] Xingang Chen and Yi Wang. Quasi-Single Field Inflation and Non-Gaussianities. JCAP, 04:027, 2010.
- [25] Clifford Cheung, Paolo Creminelli, A. Liam Fitzpatrick, Jared Kaplan, and Leonardo Senatore. The Effective Field Theory of Inflation. *JHEP*, 03:014, 2008.
- [26] J. Chluba and R. A. Sunyaev. The evolution of CMB spectral distortions in the early Universe. Mon. Not. Roy. Astron. Soc., 419:1294–1314, 2012.
- [27] Jens Chluba. Distinguishing different scenarios of early energy release with spectral distortions of the cosmic microwave background. Mon. Not. Roy. Astron. Soc., 436:2232–2243, 2013.
- [28] Jens Chluba. Which spectral distortions does ACDM actually predict? Mon. Not. Roy. Astron. Soc., 460(1):227–239, 2016.
- [29] Jens Chluba, Emanuela Dimastrogiovanni, Mustafa A. Amin, and Marc Kamionkowski. Evolution of CMB spectral distortion anisotropies and tests of primordial non-Gaussianity. Mon. Not. Roy. Astron. Soc., 466(2):2390–2401, 2017.
- [30] Jens Chluba, Adrienne L. Erickcek, and Ido Ben-Dayan. Probing the inflaton: Small-scale power spectrum constraints from measurements of the CMB energy spectrum. Astrophys. J., 758:76, 2012.
- [31] Jens Chluba, Rishi Khatri, and Rashid A. Sunyaev. CMB at 2x2 order: The dissipation of primordial acoustic waves and the observable part of the associated energy release. Mon. Not. Roy. Astron. Soc., 425:1129–1169, 2012.
- [32] Jens Chluba, Andrea Ravenni, and Thomas Kite. Spectro-spatial evolution of the CMB II: generalised Boltzmann hierarchy. 10 2022.
- [33] Paolo Creminelli and Matias Zaldarriaga. Single-Field Consistency Relation for the 3-Point Function. JCAP, 0410:006, 2004.
- [34] Sera Cremonini, Zygmunt Lalak, and Krzysztof Turzynski. Strongly Coupled Perturbations in Two-Field Inflationary Models. JCAP, 03:016, 2011.
- [35] Neal Dalal, Olivier Dore, Dragan Huterer, and Alexander Shirokov. The imprints of primordial non-gaussianities on large-scale structure: scale dependent bias and abundance of virialized objects. *Phys. Rev. D*, 77:123514, 2008.
- [36] R. A. Daly. Spectral distortions of the microwave background radiation resulting from the damping of pressure waves. Astrophys. J., 371, 1991.
- [37] J. Delabrouille et al. The pre-launch Planck Sky Model: a model of sky emission at submillimetre to centimetre wavelengths. Astron. Astrophys., 553:A96, 2013.
- [38] Karia R. Dibert et al. Forecasting ground-based sensitivity to the Rayleigh scattering of the CMB

- in the presence of astrophysical foregrounds. *Phys. Rev. D*, 106(6):063502, 2022.
- [39] Emanuela Dimastrogiovanni and Razieh Emami. Correlating CMB Spectral Distortions with Temperature: what do we learn on Inflation? JCAP, 12:015, 2016.
- [40] Olivier Doré et al. Cosmology with the SPHEREX All-Sky Spectral Survey. 12 2014.
- [41] Razieh Emami. Probing the Running of Primordial Bispectrum and Trispectrum using CMB Spectral Distortions. Phys. Rev. D, 100(8):083021, 2019.
- [42] Jonathan Ganc and Eiichiro Komatsu. Scale-dependent bias of galaxies and mu-type distortion of the cosmic microwave background spectrum from single-field inflation with a modified initial state. *Phys. Rev. D*, 86:023518, 2012.
- [43] E. M. George et al. A measurement of secondary cosmic microwave background anisotropies from the 2500-square-degree SPT-SZ survey. Astrophys. J., 799(2):177, 2015.
- [44] S. W. Henderson et al. Advanced ACTPol Cryogenic Detector Arrays and Readout. J. Low Temp. Phys., 184(3-4):772-779, 2016.
- [45] Wayne Hu, Douglas Scott, and Joseph Silk. Power spectrum constraints from spectral distortions in the cosmic microwave background. Astrophys. J. Lett., 430:L5–L8, 1994.
- [46] Wayne Hu and Joseph Silk. Thermalization and spectral distortions of the cosmic background radiation. Phys. Rev. D, 48:485–502, 1993.
- [47] Alba Kalaja, P. Daniel Meerburg, Guilherme L. Pimentel, and William R. Coulton. Fundamental limits on constraining primordial non-Gaussianity. *JCAP*, 04:050, 2021.
- [48] Rishi Khatri and Rashid Sunyaev. Constraints on μ-distortion fluctuations and primordial non-Gaussianity from Planck data. JCAP, 09:026, 2015.
- [49] Rishi Khatri, Rashid A. Sunyaev, and Jens Chluba. Mixing of blackbodies: entropy production and dissipation of sound waves in the early Universe. Astron. Astrophys., 543:A136, 2012.
- [50] Thomas Kite, Andrea Ravenni, Subodh P. Patil, and Jens Chluba. Bridging the gap: spectral distortions meet gravitational waves. Mon. Not. Roy. Astron. Soc., 505(3):4396, 2021.
- [51] Alan Kogut et al. ARCADE: Absolute Radiometer for Cosmology, Astrophysics, and Diffuse Emission. New Astron. Rev., 50:925–931, 2006.
- [52] Alan J. Kogut et al. The Primordial Inflation Explorer (PIXIE) Mission. Proc. SPIE Int. Soc. Opt. Eng., 7731:77311S, 2010.
- [53] Chao-Lin Kuo. Assessments of Ali, Dome A, and Summit Camp for Mm-wave Observations Using MERRA-2 Reanalysis. Astrophys. J., 848(1):64, 2017.
- [54] Oliver P. Lay and Nils W. Halverson. The impact of atmospheric fluctuations on degree-scale imaging of the cosmic microwave background. Astrophys. J., 543:787–798, 2000.
- [55] Antony Lewis, Anthony Challinor, and Anthony Lasenby. Efficient computation of CMB anisotropies

- in closed FRW models. Astrophys. J., 538:473-476, 2000
- [56] Juan Martin Maldacena. Non-Gaussian features of primordial fluctuations in single field inflationary models. *JHEP*, 05:013, 2003.
- [57] John C. Mather et al. Measurement of the Cosmic Microwave Background spectrum by the COBE FI-RAS instrument. Astrophys. J., 420:439–444, 1994.
- [58] Thomas W. Morris et al. The Atacama Cosmology Telescope: Modeling bulk atmospheric motion. Phys. Rev. D, 105(4):042004, 2022.
- [59] Giorgio Orlando, P. Daniel Meerburg, and Subodh P. Patil. Primordial tensor bispectra in μ -CMB cross-correlations. JCAP, 02(02):004, 2022.
- [60] Ogan Özsoy and Gianmassimo Tasinato. CMB μT cross correlations as a probe of primordial black hole scenarios. Phys. Rev. D, 104(4):043526, 2021.
- [61] Enrico Pajer and Matias Zaldarriaga. A New Window on Primordial non-Gaussianity. Phys. Rev. Lett., 109:021302, 2012.
- [62] Andrea Ravenni, Michele Liguori, Nicola Bartolo, and Maresuke Shiraishi. Primordial non-Gaussianity with μ-type and y-type spectral distortions: exploiting Cosmic Microwave Background polarization and dealing with secondary sources. JCAP, 09:042, 2017.
- [63] M. Remazeilles and J. Chluba. Extracting foreground-obscured μ-distortion anisotropies to constrain primordial non-Gaussianity. Mon. Not. Roy. Astron. Soc., 478(1):807–824, 2018.
- [64] Mathieu Remazeilles, Jacques Delabrouille, and Jean-Francois Cardoso. CMB and SZ effect separation with Constrained Internal Linear Combinations. Mon. Not. Roy. Astron. Soc., 410:2481, 2011.
- [65] Mathieu Remazeilles, Andrea Ravenni, and Jens Chluba. Leverage on small-scale primordial non-Gaussianity through cross-correlations between CMB E-mode and μ-distortion anisotropies. Mon. Not. Roy. Astron. Soc., 512(1):455–470, 2022.
- [66] Aditya Rotti, Andrea Ravenni, and Jens Chluba. Non-Gaussianity constraints with anisotropic μ distortion measurements from Planck. Mon. Not. Roy. Astron. Soc., 515(4):5847–5868, 2022.
- [67] Leonardo Senatore, Kendrick M. Smith, and Matias Zaldarriaga. Non-Gaussianities in Single Field Inflation and their Optimal Limits from the WMAP 5-year Data. JCAP, 01:028, 2010.
- [68] Joseph Silk. Cosmic black body radiation and galaxy formation. *Astrophys. J.*, 151:459–471, 1968.
- [69] Eva Silverstein and David Tong. Scalar speed limits and cosmology: Acceleration from D-cceleration. Phys. Rev. D, 70:103505, 2004.
- [70] Kendrick M. Smith, Marilena LoVerde, and Matias Zaldarriaga. A universal bound on N-point correlations from inflation. *Phys. Rev. Lett.*, 107:191301, 2011.
- [71] J. A. Sobrin et al. The Design and Integrated Performance of SPT-3G. Astrophys. J. Supp., 258(2):42, 2022
- [72] K. T. Story et al. A Measurement of the Cosmic Microwave Background Damping Tail from the 2500-

- square-degree SPT-SZ survey. Astrophys. J., 779:86, 2013.
- [73] R. A. Sunyaev and Ya. B. Zeldovich. Small scale entropy and adiabatic density perturbations? Antimatter in the Universe. Astrophys. Space Sci., 9(3):368–382, 1970.
- [74] R. A. Sunyaev and Ya. B. Zeldovich. The Interaction of matter and radiation in the hot model of the universe. Astrophys. Space Sci., 7:20–30, 1970.
- [75] Ben Thorne, Jo Dunkley, David Alonso, and Sigurd Naess. The Python Sky Model: software for simulating the Galactic microwave sky. Mon. Not. Roy. Astron. Soc., 469(3):2821–2833, 2017.
- [76] Andrew J. Tolley and Mark Wyman. The Gelaton Scenario: Equilateral non-Gaussianity from multi-

- field dynamics. Phys. Rev. D, 81:043502, 2010.
- [77] A. Weltman et al. Fundamental physics with the Square Kilometre Array. Publ. Astron. Soc. Austral., 37:e002, 2020.
- [78] R. L. Workman et al. Review of Particle Physics. PTEP, 2022:083C01, 2022.
- [79] David Zegeye, Keisuke Inomata, and Wayne Hu. Spectral distortion anisotropy from inflation for primordial black holes. *Phys. Rev. D*, 105(10):103535, 2022.
- [80] Ya. B. Zeldovich and R. A. Sunyaev. The Interaction of Matter and Radiation in a Hot-Model Universe. Astrophys. Space Sci., 4:301–316, 1969.